RESEARCH ARTICLE

Predicting the Thermal Behavior in Functional Textile Fibers Having Embedded Electronics

Shaun Berry[1] · Shawn Redmond[1] · Tairan Wang[1] · Mordechai Rothschild[1]

Abstract

In this paper, both steady-state and transient thermal simulations were performed on functional fibers having an embedded electronic chip acting as a heat source. Simulations were conducted for a range of different fiber materials and arbitrary fiber cross-sectional shapes. We show that under steady-state heating conditions, the thermal response for any arbitrary fiber shape and fiber material system was convection dominated regardless of the effective thermal conductivity of the fiber, and that the corresponding temperature rise within the fiber can be predicted analytically allowing for the maximum temperature to be estimated for any known heat load and fiber geometry. In the case of transient heating, we show that for pulsed power operation of the embedded electronic device, the maximum temperature reached in the fiber is always greater than the maximum temperature of the equivalent steady-state average power. However, high peak powers can be safely achieved if the power-on pulse time and duty cycle are selected to limit the maximum temperature reached in the fiber. Based on the results from the transient simulations, a set of criteria was developed to determine whether the operating conditions would be: (1) allowable for the fiber system, thus requiring no transient simulations, (2) requiring a transient simulation to verify that the maximum temperature is acceptable, and (3) the operating conditions are too severe and device operation at these conditions are not practical.

Introduction

The field of functional fibers and fabrics is growing rapidly, driven in part by advancements in fabrication methods that allow for heterogeneous integration of microelectronic and optoelectronic devices in fibers coupled with the ability to power such devices and communicate with them via conductive wires, also embedded in the fibers [1–4]. Applications of such a fiber architecture span the range from distributed chemical and fluidic sensors [5, 6], physiological status monitoring sensors [7, 8], optical communications [9], energy harvesting [10–14], color changing [15], and more. The devices incorporated in fibers include light emitting diodes (LEDs) [16, 17], photodetecting diodes [18], temperature sensors [19], pressure sensors [20–23], even radio-frequency (RF) devices and antennas [24, 25]. Miniaturized,

low-power devices are continuously being introduced with improved performance, including their associated integrated ultralow-power control and readout circuitry [26]. This general trend in the field of micro-opto-electromechanical system (MOEMS) further provides impetus to the coupling of such devices with the rejuvenated field of functional textiles.

The need to understand material behavior of these functional fibers will be critical as new applications continue to grow. A major part of this understanding will be the thermal management of the heat generated from the operation of embedded electronics. It is to be expected that any active MOEMS devices will generate some amount of heat, depending on the power requirements, device efficiency, and device density. However, the resulting temperature rise, whether locally in the immediate vicinity of the device or even at some distance from it, is rarely of secondary concern. In fact, it may prove to be the limiting consideration in the scale-up and even the very utility of many fiber-based system applications, as it may be detrimental to the operation of functional fibers. Excessive temperature rise can lead to failure of the electronic device, the fiber, or both. In some

---

✉ Shaun Berry
  sberry@LL.mit.edu

1 MIT Lincoln Laboratory, 244 Wood Street, Lexington,
   MA 02421, USA

applications knowing the temperature rise within the fiber is critical because it can have adverse effects on the surrounding ambient. For example, functional fibers have the potential to be used in Optogenetics [27, 28] given fiber sizes and ability to address embedded LED's, and photodiodes. For any in vivo techniques in this field, brain cells can only tolerate small changes in temperature (< 1 °C) before cellular damage [29, 30]. Thus, any heat generated from either the light emitting device(s) and/or light collecting device(s) within the fibers and the resulting temperature profile has to be well understood.

Performing a detailed thermal analysis early in the design cycle is critical for identifying the limiting operating conditions. Such an analysis will provide guidelines for the choice of materials, fiber geometry, and suitable thermal management, as well as identifying limiting operational conditions of power, size, and device density. However, detailed thermal modeling often requires specialized individuals to conduct these types of analyses, as well as dedicated software that might not be readily available for many researchers and designers working in this field. The goal of this work is to understand the thermal behavior in functional fibers consisting of different materials, and arbitrary shapes, under different heating loads and ambient environments to: (1) gain a greater understanding of what parameters affect thermal management in these types of systems and (2) to see if predictive analytical models can be found that estimate the expected temperature profile, making complex numerical modeling unnecessary. To this end, we created detailed finite element thermal models of a single-fiber/single-device case, with extension to the single-fiber/multiple-device case, leaving more complex analysis of two-dimensional networks to a later effort. Both steady-state and transient thermal simulations were performed.

Thermal Modeling

High-fidelity, three-dimensional finite element models were created for a single fiber having a single heat source. The generalized heat equation was solved using COMSOL Multiphysics (ver. 5.4). Figure 1 shows the typical functional fiber geometry simulated. It consists of a thermally drawn polycarbonate fiber with an embedded electronic device, simulated as a silicon chip that will provide the heat source, and two copper wires that provide power. The thermal draw from a preformed process of multimaterial fibers is described in [3, 4, 31]. In these simulations, only polycarbonate and copper wires were modeled in the material selection. However, it should be noted that the thermal-draw process allows for a large selection of materials to be formed into a fiber. At the Defense Fabric Discovery Center (DFDC) at MIT Lincoln Laboratory, fibers have been drawn, in addition to polycarbonate, from: polyetherimide (PEI), polyvinylidene
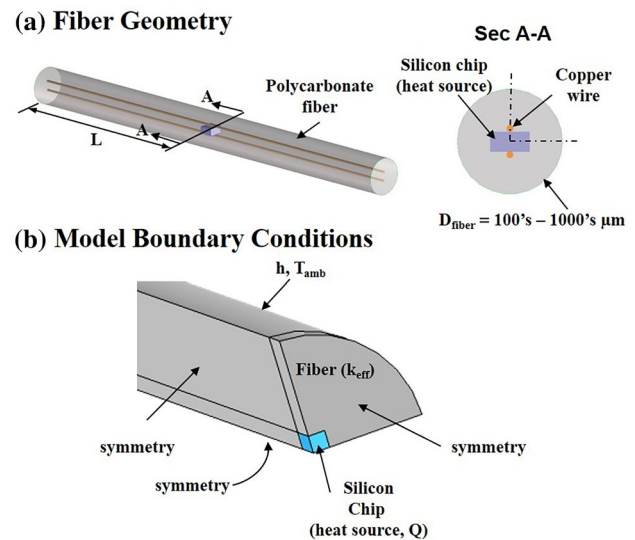

(a) Fiber Geometry

Sec A-A

Polycarbonate fiber

Silicon chip (heat source)

Copper wire

$D_{fiber} = $ 100's – 1000's μm

(b) Model Boundary Conditions

h, T_{amb}

Fiber (k_{eff})

symmetry

symmetry

symmetry

Silicon Chip (heat source, Q)

Fig. 1 **a** Representative functional fiber geometry with an embedded device and two metal conductive wires. **b** Geometry having symmetry planes that was discretized into finite elements and the associated boundary conditions used in the thermal simulations

fluoride (PVDF), polyethylene (PE), cyclic olefin copolymer (COC) and poly(methyl methacrylate) (PMMA) to name a few. Also, other common materials such as copper wires, aluminum wires, tungsten wire, Kevlar, and Vectran have been co-drawn with the polymer fibers. Though just a single material set was used in these simulations, as will be shown, the trends observed from the simulations are relatively independent of the absolute materials properties being modeled.

The primary cross-sectional shape modeled was circular. However, other cross-sectional geometries were also investigated. Where applicable, geometric symmetry planes were utilized to help reduce the number of finite elements in the model.

To further simplify model construction and rapidly evaluate different input variables, effective material properties were used instead of explicitly modeling the wire geometry embedded in the polymer fiber. For example, the effective thermal conductivity was defined as

$$k_{eff} = \frac{A_w}{A_c} k_{wire} + \frac{A_f}{A_c} k_{fiber}, \tag{1}$$

where A_c is the total cross-sectional area of the fiber geometry, A_w the total cross-sectional area of the metal wires, k_{wire} the thermal conductivity of the metal wires, k_{fiber} the thermal conductivity of the fiber material, and A_f the cross-sectional area of just the fiber material and can be found from $A_f = A_c - A_w$. Effective density and the effective specific heat were also calculated in a similar manner. Table 1 lists the material properties used in these simulations. It should be noted that

Table 1 Material properties

Material	Density (kg/m³)	Thermal conductivity (W/m °C)	Specific heat (J/kg K)
Polycarbonate [32]	1200	0.2	1250
Copper [33]	8960	400	385

the material properties were assumed to be constant, and we did not consider their variations with temperature. Over our temperature range of interest, the variations are relatively small, and they can be incorporated in future refinements of the model.

The fiber length was defined from the center of the embedded chip (longitudinal symmetry plane in the model) to a free end. The fiber length was assumed to be long enough to ensure no heat loss from the free end. This fiber length was determined from the theory of heat transfer for extended surfaces [33] and given as

$$L_\infty = 2.65 \left(\frac{k_{eff} A_c}{hP} \right)^{1/2},$$ (2)

where k_{eff} is the effective thermal conductivity, A_c the total fiber cross-sectional area, h the heat transfer coefficient and P the fiber cross section perimeter. For a circular cross section with diameter D_f, the above expression reduces to: $L_\infty = 1.325 \, (k_{eff} D_f/h)^{1/2}$.

The boundary condition at the fiber free end was defined as adiabatic, meaning that there was no heat flux across that boundary. The boundary condition along the perimeter of the fiber was defined as a convective heat flux to the surrounding

ambient environment, set by the heat transfer coefficient, h, and ambient temperature, T_{amb}. Power from the chip was applied as a volumetric heat source defined as Q_o/V, having units of W/m³, where Q_o is the heat from the chip and was one of the input variables in these simulations, and V is the volume of the chip. For consistency, the chip volume was kept the same in all simulations with dimensions of width = 150 μm, length = 300 μm, and thickness = 150 μm.

Simulations were conducted for different fiber diameters, different effective thermal conductivities, k_{eff}, heat transfer coefficients, h, and heat inputs, Q_o. The fiber diameters evaluated were $D_f = 250$ μm, 500 μm, 1000 μm and 1500 μm, which are the range of sizes of fibers that are currently being developed for many functional fiber applications. The effective thermal conductivities were determined from the area ratios of copper wire to fiber, defined as A_w/A_f. Values of 0.0, 0.01, 0.1, 0.5 and 1.0 were used. For example, when $A_w/A_f = 0$, the entire fiber is all polymer, and $k_{eff} = 0.2$ W/(m K). When $A_w/A_f = 1$, the entire fiber is all copper, and $k_{eff} = 400$ W/(m K).

Thermal Simulation Results

Steady-State Simulations

An example of the results generated from the steady-state simulations is shown in Fig. 2, which shows the temperature contours in a 500-μm diameter fiber having an area ratio of $A_w/A_f = 0.01$, chip heat of $Q_o = 10$ mW, and $h = 5$ W/(m² K). For this area ratio, $k_{eff} = 4.2$ W/(m K).

As expected, the maximum temperature was located at the cross-sectional plane through the center of the heat

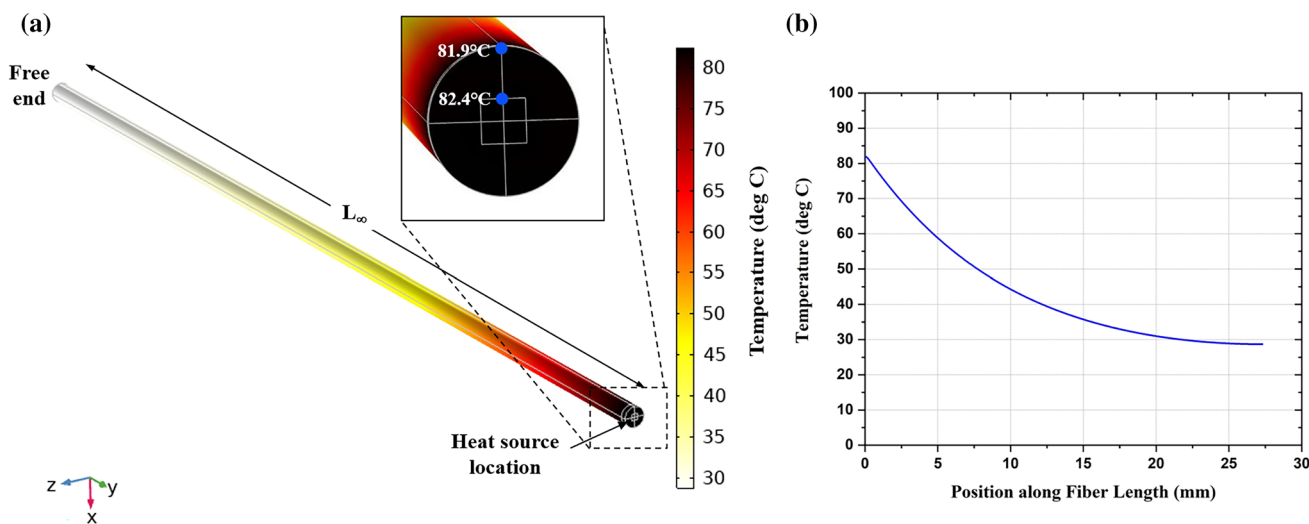**Fig. 2** **a** Temperature contour plot for a 500-μm diameter polycarbonate fiber under the following conditions: $Q_o = 10$ mW, $k_{eff} = 4.2$ W/(m K), $h = 5$ W/(m² K) and $T_{amb} = 20$ °C. $T_{max} = 82$ °C. **b** Temperature profile along the length of the fiber

source. The temperature in the fiber decays from the heat source, along the length of the fiber, from T_{max} to a T_{min} value (Fig. 2b), and follows the same temperature distribution derived for extended surfaces having an adiabatic free end [33],

$$T(x) = \frac{\cosh\left(m(L_\infty - x)\right)}{\cosh\left(mL_\infty\right)}\left[T_{max} - T_{amb}\right] + T_{amb}, \quad (3)$$

where $m = \sqrt{\frac{hP}{k_{eff}A_c}}$. Equation 3 is valid as long as the heat sources are spaced at $2 \times L_\infty$, which will be discussed later in this section, as well as determining T_{max}. The temperature profile at any cross section of the fiber was observed to be uniform through the thickness of the fiber. The uniform temperature through the fiber cross section indicates that heat transfer is dominated by convection to the ambient, and not conduction within the fiber. In conduction problems that involve surface convection effects, the Biot number, a dimensionless parameter, can be used to estimate when the condition for uniform temperature distribution exists for a functional fiber design. The Biot number is defined by

$$Bi = \frac{hL_c}{k_{eff}}, \quad (4)$$

where L_c is a characteristic length, and for an infinite long circular fiber, equal to $D_f/2$. In general, systems with small Biot numbers, $Bi < 0.1$, are simpler to find analytical expressions for the temperature field, since the fields are uniform through the body. When $Bi > 0.1$, a uniform temperature profile can no longer be assumed, the temperature distribution across the fiber will be non-linear, and often can only be determined through numerical simulations. For most of the functional fiber sizes being evaluated in this paper, the Biot values were found to be much less than 0.1 ($Bi << 0.1$), meaning the temperature profiles through the fiber cross section were uniform and dominated by convection at the surface. The few exceptions to this were for the fiber sizes with $D_f \geq 1$ mm, $h \geq 50$ W/(m^2 K) and having $k_{eff} \leq 0.2$ W/(m K). For cases when $k_{eff} > 0.2$ W/(m K), the Biot number was much less than 0.1 for all the fiber sizes and heat transfer coefficients evaluated. Having uniform temperature profiles through the fiber cross section will be important for estimating the temperature rise in the fiber without the need for numerical simulation, as will be discussed later in this section.

However, even for small Bi numbers, the effective thermal conductivity does have a role in the maximum temperature the fiber will experience. Figure 3 plots ΔT_{max}, defined as $T_{max} - T_{amb}$, vs. A_w/A_f, for $D_f = 500$ μm, $Q_o = 10$ mW, and $h = 5$ W/(m^2 K), leading to $Bi << 0.1$ for all the modeling conditions.

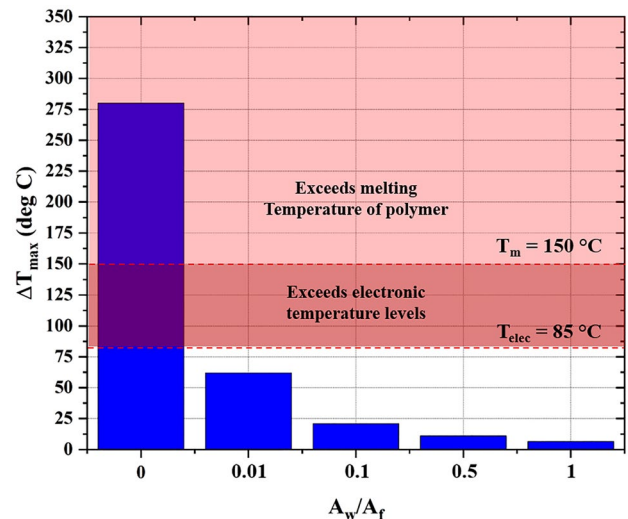**Fig. 3** ΔT_{max} vs. A_w/A_f, for a 500-μm diameter polycarbonate fiber, under the following conditions: $Q_o = 10$ mW, $h = 5$ W/(m^2 K) and $T_{amb} = 20$ °C

The influence of the effective thermal conductivity on the maximum temperature that is reached in the fiber can be seen by the reduction in ΔT_{max} as A_w/A_f increases. As the results show, a 500-μm diameter fiber that is all polycarbonate, $A_w/A_f = 0$ and $k_{eff} = 0.2$ W/(m K), would develop temperatures that exceed the melting point of the polycarbonate from only 10 mW of heat. However, if the fiber included a single copper wire having a diameter of 50 μm, leading to $A_w/A_f = 0.01$ and $k_{eff} = 4.2$ W/(m K), ΔT_{max} is now below the limiting operating temperature for most electronics, which is commonly assumed to be 85 °C for industrial applications [34].

The results in Fig. 3 refer to a specific set of parameters. In practice, it is helpful to have a generalized set of data, which can provide guidance under a broad range of experimental conditions. To compare the results for all the other fibers sizes, ambient conditions, and material properties that were simulated, the results were normalized so that a single generalized plot was found that defines the thermal response for any arbitrary functional fiber shape. First, we define the effective thermal resistance as $\Delta T_{max}/Q_o$. Using this parameter, we can scale the maximum temperature rise at any heat power levels. Next, we define the fiber surface area based on the theory of heat transfer for extended surfaces [33], as $A_s = P \cdot L_\infty$. By plotting the effective thermal resistance of a fiber vs. the fiber surface area, A_s, one obtains near-universal curves independent of the fiber diameter or the ratio of conductive wire to fiber. The data points represent simulation results for the four different fiber sizes and the five different copper wire-to-fiber area ratios (0, 0.01, 0.1, 0.5 and 1), for $h = 5$, 50 and 500 W/(m^2 K).
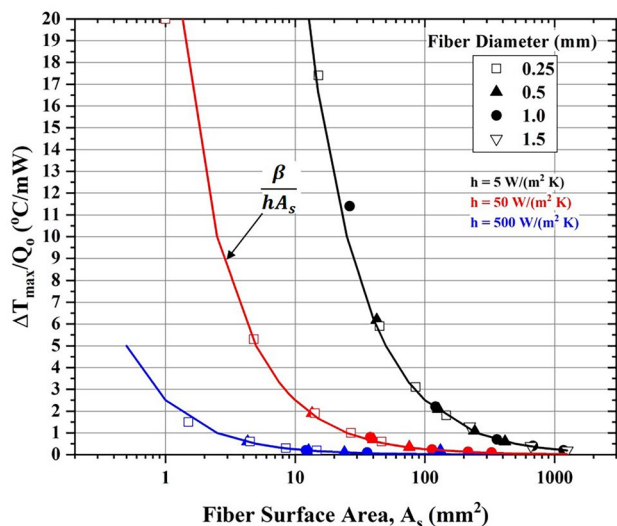
Fig. 4 Effective thermal resistance, $\Delta T_{max}/Q_o$ vs. the fiber surface area, A_s for different values of heat transfer coefficients, h. A_s is defined as the perimeter of the fiber, P, times L_∞. The data points are results from numerical simulations. The solid lines represent the fiber thermal resistance determined from convection, including a correction factor $\beta = 1.25$ due to thermal conductivity effects

Figure 4 illustrates the effect on thermal resistance of varying h and k_{eff}. The results show that even when everything else is normalized, the parameter h is a powerful independent variable. Also shown are "universal" curves for three values of h: 5 W/(m² K), corresponding to stagnant air; 50 W/(m² K), corresponding to stagnant water as ambient; and 500 W/(m² K), corresponding to actively cooled air ambient, such as in the presence of a fan. As expected from a convection dominated system, the thermal resistance is nearly inversely proportional to h.

The "universal" curves are calculated assuming effective thermal resistance must be equal to thermal resistance due to convection. From heat transfer theory, the thermal resistance due to convection is given by; $R_{conv} = \frac{1}{hA_s}$. This is an idealization that assumes the entire length of the fiber is at ΔT_{max}. However, since there is a temperature gradient along the length of the fiber from the heat source to the end of the fiber, there is an effect from the resistance due to thermal conductivity on maximum temperature in the fiber that needs to be accounted for. Based on all the simulations that were conducted, adjusting R_{conv} by a factor of 1.25 was found to approximately equal the effective thermal resistance as determined form the simulation data. Figure 4 shows the thermal resistance due to convection with the parameter $\beta = 1.25$, plotted with the simulation results (solid lines). This rationale for a correction factor can also be found in other one-dimensional heat transfer applications such as extended surfaces.

The results from Fig. 4 also indicate that developing high thermal conductivity materials for functional fibers can provide thermal management assistance even for a system dominated by convection. As Eq. 2 indicates, L_∞ gets larger for increases in k_{eff}, therefore increasing A_s and thus reducing the effective thermal resistance, which generally means devices can operate at higher heat loads. However, one must keep in mind that increasing k_{eff} means that the thermal zone of influence of the device increases along the fiber, necessitating a longer fiber and spacing between devices. The effect of increasing thermal conductivity, either by adding more wires to the fiber, or reducing the fiber diameter, or increasing the conductivity of the fiber material, is deduced from the impact of changes in k_{eff} on A_s in Fig. 4, in combination with Eq. 2.

Additionally, one may consider changing the cross-sectional shape of the fiber to increase its perimeter P while keeping the area constant. Since $A_s = P \cdot L_\infty$ and L_∞ is dependent on P as the inverse square root, the net effect is a sublinear reduction in thermal resistance. Indeed, Fig. 5 confirms that arbitrary-shaped fibers are expected to obey the same universal trends as circular fibers. Both a rectangular cross-sectional shape and a radially finned shape were modeled, in addition to the circular fiber geometry. It should be noted that because of the thermal draw from a performed fabrication process, nearly any arbitrary cross-sectional shape can be potentially drawn into a fiber as long as the shape can be made in a larger preform. While circular and rectangular
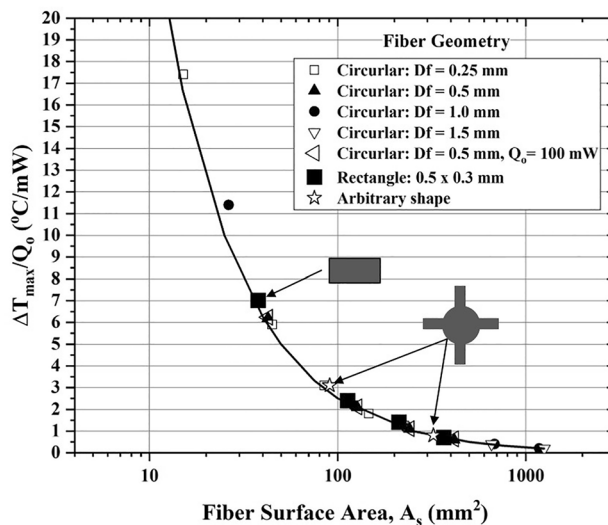

Fig. 5 Effective thermal resistance, $\Delta T_{max}/Q_o$ vs. the fiber surface area, A_s for different fiber cross sections for $h = 5$ W/(m² K). Data points are from numerical simulations. The solid lines represent the fiber thermal resistance determined from convection. The arbitrary shape in this plot was a radially finned shape consisted of circular center having a diameter of 0.5 mm and each fin width = 0.1 mm and fin height = 0.5 mm

fiber cross sections are the most common, more exotic shapes are achievable, like the radially finned shape that was chosen here to illustrate that regardless of shape, heat transfer in these systems are convection dominated.

Furthermore, the spacing between discrete devices can greatly influence the temperature in the fiber. The value of L_∞ defines the minimal separation between discrete devices required for negligible thermal cross talk between such devices. For instance, for $k_{eff} = 4$ W/(m K), $h = 5$ W/(m² K), which is a typical value used for stagnant air, and $D_f = 500$ μm, the minimal device separation should be ~5 cm, which is $2 \times L_\infty$. Although $2 \times L_\infty$ defines the minimal distance for devices to be spaced for the lowest operating temperatures to be reached, discrete devices can be spaced at higher densities depending on the operating conditions. To evaluate the effect of device density, steady-state simulations were performed where heat sources were spaced at locations $< 2 \times L_\infty$. Figure 6 plots ΔT_{max} normalized by the maximum temperature for a device spaced at $2 \times L_\infty$ vs. the distance between devices normalized by $2 \times L_\infty$ for different values of k_{eff} for a fiber system of $D_f = 500$ μm, $h = 5$ W/(m² K), and $Q_o = 10$ mW.

The trends in results in Fig. 6 were typical for other fiber systems simulated. The results indicate that as the spacing between devices gets closer, the maximum temperature in the fiber increases for a constant set of operating conditions. A more than threefold increase in the maximum temperature can result when devices are spaced at $\leq 10\%$ of $2 \times L_\infty$. However, depending on the operating conditions and the temperature limits are for a specific application, it will be practical to have devices spaced at distances $<< 2 \times L_\infty$, especially in systems with high thermal conductivity.
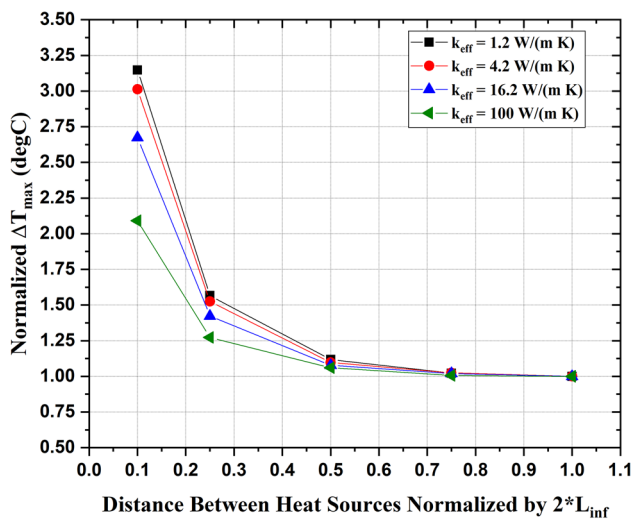

Fig. 6 ΔT_{max} normalized by the maximum ΔT_{max} for a device spacing of $2 \times L_\infty$ vs. the distance between devices normalized by $2 \times L_\infty$ for different values of k_{eff} for a fiber system of $D_f = 500$ μm, $h = 5$ W/(m² K), and $Q_o = 10$ mW

Based on the steady-state thermal modeling analysis results, and the "universal" trends observed, the maximum temperature rise in a functional fiber that has heat generating embedded electronic devices, regardless of cross-sectional shape, can be analytically predicted. For functional fiber systems having Bi < 0.1, the maximum expected temperature can be estimated from,

$$T_{max} = Q_o \left(\frac{\beta}{hA_s} \right) + T_{amb}, \tag{5}$$

where $\beta = 1.25$ for the fiber sizes, and conditions evaluated in this modeling work. For functional fibers operating in stagnant air, A_s is commonly in the range 25–100 mm² and therefore the effective thermal resistance is ~2 to 10 °C/mW. Assuming $T_{amb} = 20$ °C and maximum operating temperature of 85 °C, i.e., $\Delta T_{max} = 65$ °C, the allowable heat generation for steady-state operation of the embedded device is ~5 to 30 mW. These values bound the operating range of embedded devices and provide guidance to the limitations of various envisioned applications of functional fibers.

Experimental Measurements

To validate both the numerical simulations and the analytical model derived from the simulations, temperature data were collected from a 1-mm diameter polycarbonate fiber having embedded LED's (CREE, C527UT170-S0400-31) spaced approximately every 50 mm apart. The functional fiber was fabricated in the DFDC using a thermal draw from a preform process. The LEDs in the fiber were electrically contacted by two 100-μm diameter copper wires. Temperature was collected using an FLIR camera for different LED operating conditions in a laboratory setting ($T_{amb} = 25$ °C, stagnant air). Figure 7a shows a visible image of the fiber and a single LED, and Fig. 7b shows the resulting IR camera image of the LED operating at 4 mA (dissipated power, $Q_o = 12$ mW). Two toothpicks were placed over the fiber, 20 mm apart to act as a distance reference in the thermal image.

Equations 1, 2 and 5 were used to estimate the maximum temperature in the fiber based on the known fiber geometry inputs, dissipated power at different LED operating conditions, and the ambient conditions. The only unknown in this analysis is the value of the average heat transfer coefficient, h, to be used in Eqs. 2 and 5. Since the fiber was operating in a controlled laboratory setting, values of $h = 5$, 10 and 20 W/(m² K) were used in the calculations to bound the stagnant air flow convection range and see the effect on the calculated maximum temperature over that range. Figure 8a shows the measured maximum temperature in the fiber as a function of dissipated LED power (Q_o), and the estimated
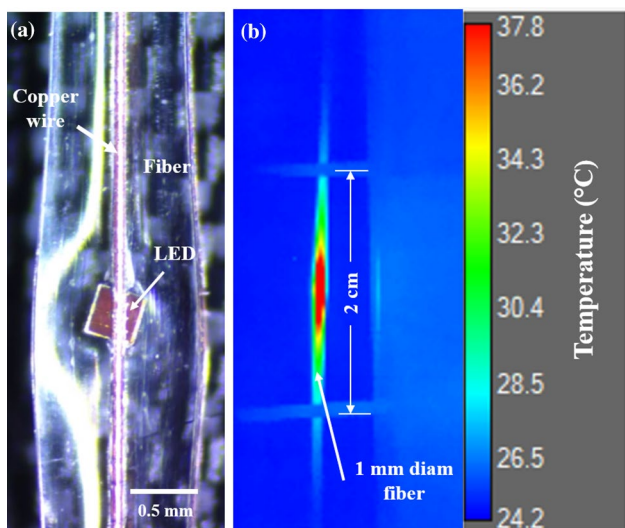
Fig. 7 a 1-mm diameter polycarbonate fiber with embedded LED contacted by two 100-μm diameter copper wires. One wire is above the LED the other is below the LED. Image courtesy of the Defense Fabric Discovery Center at MIT Lincoln Laboratory. **b** Thermal image collected from IR camera for the LED operating at 4 mA (12 mW dissipated power)

maximum temperature based on Eq. 5, under steady-state operation. Figure 8b lists the known and calculated parameters for $h = 10$ W/(m² K), and Fig. 8c lists the actual measured maximum temperature and calculated maximum temperature using Eq. 5 for $h = 10$ W/(m² K).

As the results show, Eq. 5 can accurately estimate the maximum temperature in the fiber resulting from an embedded heat source, confirming that in these fiber systems for Bi < 0.1, heat transfer is convection dominated. If the model input parameters, especially the heat transfer coefficient are well understood, the absolute maximum temperature in the fiber can be predicted with great accuracy. However, if the input parameters are not fully known, the problem space can be easily bound with this analytical approach helping to make design decisions.

Transient Simulations

Many electronic devices, especially MOEM devices operate with chip power pulsed at various duty cycles, often with high peak powers, relative to average operating powers. To understand what effect this type of temporal operation has on the maximum expected temperatures in functional fibers, transient numerical simulations were performed. The same modeling boundary conditions and effective material properties that were used in the steady-state simulations were also used in the transient simulations, except that chip power was applied as a function of time.

The transient simulations were done in two study steps within the same simulation. The first study was a steady-state analysis to find the temperature profile in the fiber for an average chip power that is constantly on. In the second study step, the temperatures from the steady-state analysis were then used as the initial conditions. The average
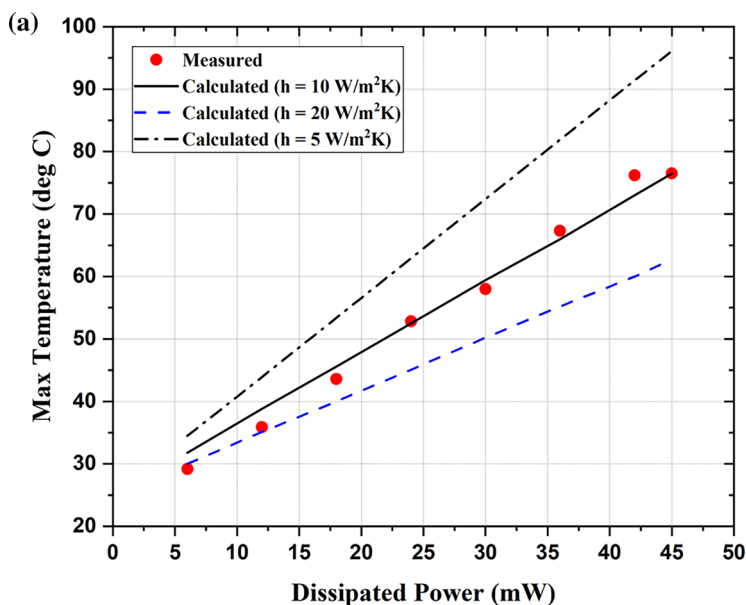
(b) Parameter	Value
D_f	1.0 mm
D_w	0.1 mm
Ac	0.784 mm²
k_{eff}	8.2 W/(m K)
P	3.142 mm
A_s	119.2 mm²
L_∞	37.9 mm

(c) Q_o (mW)	T_{max} (Measured)	T_{max} (Calculated)
6	29.2	31.8
12	35.9	38.8
18	43.6	45.6
24	52.8	52.5
30	58.0	59.4
36	67.3	66
42	76.2	73
45	76.5	76.5

Fig. 8 a Maximum temperature reached in the 1-mm diameter polycarbonate fiber vs. LED power. Data points are measured values and solid lines are calculated. **b** Table of known and calculated parameters using $h = 10$ W/(m² K). **c** Table of measured maximum temperature in the fiber and calculated maximum temperature from Eq. 5

operating power used in all the transient simulations was set at: $Q_{avg} = 10$ mW. The peak power of the chip, Q_p, was applied as a step function for a pulse time, t_{on}, and duty cycle. The duty cycle and peak power were chosen so that average power equals 10 mW.

Three different duty cycles were evaluated: 1%, 10% and 20% duty cycle. For each duty cycle, three different pulse times were simulated: 1 ms, 100 ms, and 1000 ms. For example, a 10% duty cycle translates to a peak power of $Q_p = 100$ mW, and if $t_{on} = 100$ ms, then the total time for a single pulse cycle (power on and power off) is 1000 ms. The simulations were run long enough to have at least 4-pulse cycles simulated. Just as was done in the steady-state analysis, a matrix of simulations was conducted for different fiber diameters, and different effective thermal conductivities, k_{eff}. The fiber diameters evaluated were $D_f = 250$ μm, 500 μm, 1000 μm and 1500 μm. The effective thermal conductivities and the other required material properties for transient simulation, i.e., density and specific heat, were determined from the area ratios of copper wire to fiber, defined as A_w/A_f. Area ratio values of 0.0, 0.01, 0.1, 0.5 and 1.0 were used in the simulations. Additionally, the ambient conditions assumed for all the transient simulations were $h = 5$ W/(m² K) and $T_{amb} = 20$ °C, unless noted.

An example of the typical results that are generated from a transient simulation are shown in Fig. 9, which plots ΔT_{max} vs. time for a 500-μm diameter fiber having an area ratio of $A_w/A_f = 0.01$, for two different peak powers and duty cycles. Results are for a peak power, Q_p, of 100 mW, applied for 100 ms at a 10% duty cycle and for $Q_p = 50$ mW applied for 100 ms at 20% duty cycle.

For pulsed operation where the peak power is greater than the average power, the temperature rises above the steady-state average power temperature if the power is pulsed on. The rise in temperature above steady-state is defined as ΔT_1. Once the power pulse is turned off, the temperature decays, dropping below the steady-state temperature if the off time is long enough. As can be seen in Fig. 9, the maximum temperature as a function of time will oscillate consistently about a steady-state temperature when the peak power, pulse time, and duty cycle are set so that it equals the average operating power. If the peak power was left on indefinitely, the temperature would continue to rise until reaching a new steady-state value for that power level. Using Eq. 5, the new maximum steady-state temperature can be estimated. For the set of input conditions in Fig. 9, $\Delta T_{max} = 600$ °C for $Q_p = 100$ mW, and $\Delta T_{max} = 290$ °C for $Q_p = 50$ mW. Clearly, these temperature values are unrealistic, since the melting temperature of the fiber, ~ 150 °C for polycarbonate, would have been reached for both these heating conditions. However, as the results show in Fig. 9, the rise above steady-state $\Delta T_1 \cong 10$ °C for $Q_p = 50$ mW and $\Delta T_1 \cong 25$ °C for $Q_p = 100$ mW, indicates that in pulsed operation, very high peak
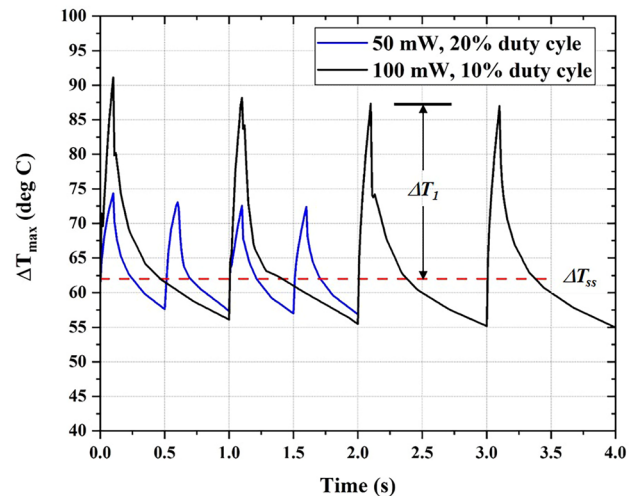

Fig. 9 ΔT_{max} vs. time for a 500-μm diameter fiber having an area ratio of $A_w/A_f = 0.1$, i.e., $k_{eff} = 4.2$ W/(m K), for two different peak powers pulsed at different duty cycles, having ambient conditions of $h = 5$ W/(m² K) and $T_{amb} = 20$ °C. The dashed line (red dashed line) represents the maximum steady-state temperature, ΔT_{ss}, from the average power of $Q_{avg} = 10$ mW

powers can be acceptable, and maximum temperatures limited, if the peak power is pulsed at the proper duty cycle and pulse time.

Predicting the maximum allowable peak power and pulse time without the need of transient thermal modeling was found to be challenging. Analytical solutions for the general heat equation having a point heat source as a function of time, which is the case for a functional fiber having discrete heat sources, exist for only specific input parameters, and not for a set of general conditions. Similarly, evaluating parameters such as the thermal capacitance, or the thermal time constant, did not provide any general predictive behavior for a broad range of fiber designs. The same was found by trying to develop an analytical model based on curve fitting the resulting temperature rise as a function of time for a given transient simulation result. These models would only be valid for that particular set of fiber inputs and heating conditions, and did not extend to different input conditions. After evaluating the matrix of transient simulations performed in this study, several relationships were observed. First, the maximum temperature rise was found to be a strong function of the peak power, Q_p, the time the power was on, and the effective material properties, namely, thermal conductivity and specific heat. Second, the rise in temperature followed a specific power input, pulse time, and thermal capacitance. Each power had its own unique ΔT_{max} vs. t curve. Third, the ambient environment, unlike for steady-state conditions, had little effect on what the temperature increase would be for short pulse times ($t_{on} \ll$ thermal time constant). Finally, as the effective specific heat decreased, meaning the effective

thermal conductivity increased, there was a decrease in ΔT_{max} for a given power and pulse time. These observations are captured in Fig. 10, which plots the delta temperature
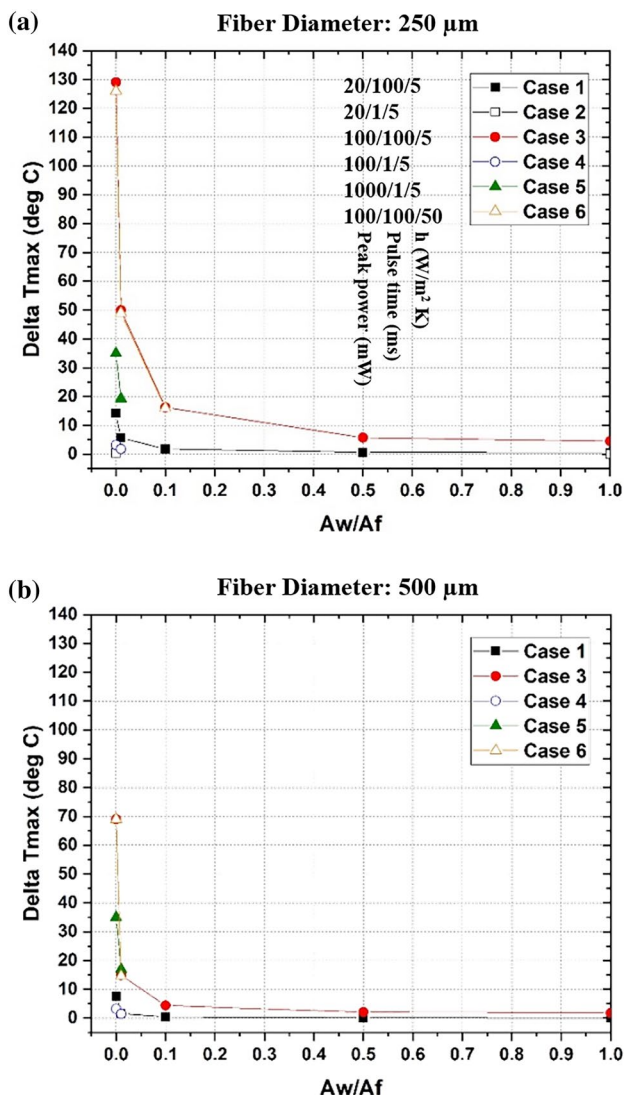
(a)

(b)

Fig. 10 ΔT_{max} above the maximum steady-state temperature vs. area ratio A_w/A_f for different power, pulse times, and ambient conditions. **a** Results for a fiber diameter of 250-μm. **b** Results for a fiber diameter of 500 μm

rise above the maximum steady-state temperature as a function of k_{eff} for different transient simulation case studies.

Based on these observations from the transient simulations, we developed a set of criteria to be used to help predict what effect high peak chip powers pulsed at various duty cycles would have. The criteria developed and the associated recommendations are presented in Table 2. It should be noted, that prior to a transient peak power evaluation, the maximum temperature from steady-state average power operation first needs to be evaluated for the fiber system.

Conclusions

The goal of this work was to understand the thermal behavior in functional fibers having embedded discrete electronic elements that produce heat. We conducted detailed numerical thermal analyses for a single functional fiber geometry that had a single heat source, and expanded it to multiple devices in a single fiber. Different fiber materials, which were modeled by varying the effective thermal conductivity of the fiber, as well as arbitrary fiber shapes were evaluated under different heating loads and ambient environments. The simulation results showed that for steady-state heating applications, the expected temperature rise follows predictive curves making numerical modeling unnecessary for a class of problems. For fiber geometries and operating conditions that produce Biot numbers, Bi < 0.1, the temperature distribution through the thickness of the fiber was observed to be uniform. The key implication of this is that heat transfer is dominated by convection to the ambient, and not conduction within the fiber, meaning the maximum temperature can be analytically determined from just the convective thermal resistance as shown in Eq. 5. Unless the operating ambient environment is well known, using values for the convective coefficient for stagnant air (2–20 W/(m² K)) will yield conservative results. For Bi >> 0.1, a non-uniform temperature profile through the fiber cross section will develop. For these conditions, numerical modeling may be necessary to accurately determine the temperature rise, especially near the heat source.

Table 2 Transient modeling criteria and recommendations

Criteria	Recommendation
Peak power ≤ 100 mW, and	No transient simulation required
Peak power pulse time (t_{on}) < 1000 ms, and	Small temperature rise above steady-state temperature
$k_{eff} \geq 40$ W/(m K), and $D_{fiber} \geq 250$ μm	Safe operating conditions for device and fiber system
Peak power > 100 mW, and	Operating conditions damaging to device or fiber system or both
Any peak power pulse time (t_{on}), and	Large temperature rise above steady-state temperature expected
$k_{eff} \leq 40$ W/(m K), and $D_{fiber} \leq 500$ μm	Device operation at these conditions not practical
All other conditions not captured in criteria 1 and criteria 2	Transient simulation recommended to confirm safe operation of device and fiber system

In the case of transient thermal simulations, pulsing the power of the heat source at different duty cycles was evaluated. A key take-away was that the maximum temperatures in pulse power operation are always greater than the maximum temperature of the equivalent steady-state average power. Additionally, if the peak power was pulsed at a time and duty cycle that equals the equivalent average operating power, then the maximum temperature will oscillate consistently about the average steady-state temperature. The transient simulation results also indicated that in pulsed operation, very high peak powers can be acceptable, and maximum temperatures limited, if the peak power is pulsed at the proper duty cycle and pulse time. Analytically determining the maximum temperature rise above the average steady-state temperature without complex numerical modeling proved challenging. However, based on the transient simulations carried out in this study, a set of design criteria was developed to assist in predicting whether operating at a particular peak power and duty cycle was acceptable for that fiber system, or if complex thermal simulations would be required.

Declarations

Conflict of Interest On behalf of all authors, the corresponding author states that there is no conflict of interest.

References

1. Yan W, Dong C, Xiang Y, Jiang S, Leber A, Loke G, Xu W, Hou C, Zhou S, Cheng M, Hu R, Shum P, Wei L, Jia X, Sorin F, Tao X, Tao G. Thermally drawn advanced functional fibers: new frontier of flexible electronics. *Mater Today* **2020**;*35*:168–94.

2. Shi Q, Sun J, Hou C, Li Y, Zhang Q, Wang H. Advanced functional fiber and smart textile. *Adv Fiber Mater* **2019**;*1*:3–31.

3. Lake G, Yan W, Khudiyev T, Noel G, Fink Y. Recent progress and perspectives of thermally drawn multimaterial fiber electronics. *Adv Mater* **2020**;*32*:1904911.

4. Wang Z, Chen M, Zheng Y, Zhang J, Wang Z, Yang J, Zhang Q, He B, Qi M, Zhang H, Li K, Wei L. Advanced thermally drawn multimaterial fibers: structure-enabled functionalities. *Adv Devices Instrum* **2021**;*2021*:9676470.

5. Gumennik A, Stolyarov A, Schell B, Hou C, Lestoquoy G, Sorin F, McDaniel W, Rose A, Joannopoulos J, Fink Y. All-in-fiber chemical sensing. *Adv Mater* **2012**;*24*(45):6005–9.

6. Dong C, Page A, Yan W, Nguyen-Dang T, Sorin F. Microstructured multimaterial fibers for microfluidic sensing. *Adv Mater Technol* **2019**;*4*:1900417.

7. Angelucci A, Cavicchioli M, Cintorrion I, Lauricella G, Rossi C, Strati S, Aliverti A. Smart textiles and sensorized garments for physiological monitoring: a review of available solutions and techniques. *Sensors* **2021**;*21*:814.

8. Loke G, Khudiyev T, Wang B, Fu S, Payra S, Shaol Y, Fung J, Chatziveroglou I, Chou P, Chinn I, Yan W, Gitelson-Kahn A, Joannopoulos J, Fink Y. Digital electronics in fibers enable fabric-based machine-learning interface. *Nat Commun* **2021**;*12*:3317.

9. Rein M, Favrod V, Hou C, Khudiyev T, Stolyarov A, Cox J, Chung C-C, Chhav C, Ellis M, Joannopoulos J, Fink Y. Diode fibers for fabric-based optical communications. *Nature* **2018**;*560*:214–8.

10. Guo Y, Dun C, Xu J, Li P, Huang W, Mu J, Hou C, Hewitt CA, Zhang Q, Li Y, Carroll DL, Wang H. Wearable thermoelectric devices based on Au-decorated two-dimensional MoS2. *ACS Appl Mater Interfaces* **2018**;*10*:33316.

11. Dong C, Leber A, Gupta T, Chandran R, Volpi M, Qu Y, Nguyen-Dang T, Bartolomei N, Yan W, Sorin F. High-efficiency super-elastic liquid metal based triboelectric fibers and textiles. *Nat Commun* **2020**;*11*:3537.

12. Chen M, Wang Z, Zhang Q, Wang Z, Liu W, Chen M, Wei L. Self-powered multifunctional sensing based on super-elastic fibers by soluble-core thermal drawing. *Nat Commun* **2021**;*12*:1416.

13. Zhang J, Zhang T, Zhang H, Wang Z, Li C, Wang Z, Li K, Huang X, Chen M, Chen Z, Tian Z, Chen H, Zhao L, Wei L. Thermoelectrics: single-crystal SnSe thermoelectric fibers via laser-induced directional crystallization: from 1D fibers to multidimensional fibers. *Adv Mater* **2020**;*32*(36):2070271.

14. Feng Z, Yang S, Jia S, Zhang Y, Jiang S, Yu L, Li R, Song G, Wang A, Martin T, Zuo L, Jia X. Scalable, washable and lightweight triboelectric-energy-generating fibers by thermal drawing process for industrial loom weaving. *Nano Energy* **2020**;*74*:104805.

15. Zhou Y, Fang J, Wang H, Zhou H, Yan G, Zhao Y, Dai L, Lin T. Multicolor electrochromic fibers with helix-patterned electrodes. *Adv Electron Mater* **2018**;*4*:1800104.

16. Kwon S, Kim W, Kim H, Choi S, Park B-C, Kang S-H, Choi K. High luminance fiber-based polymer light-emitting devices by a dip-coating method. *Adv Electron Mater* **2015**;*1*(9):1500103.

17. O'Connor B, An K, Zhao Y, Pipe K, Shtein M. Fiber shaped light emitting device. *Adv Mater* **2007**;*19*(22):3897–900.

18. Bayindir M, Sorin F, Abouraddy A, Viens J, Hart S, Joannopoulos J, Fink Y. Metal-insulator-semiconductor optoelectronic fibers. *Nature* **2004**;*431*:826–9.

19. Bayindir M, Abouraddy A, Arnold J, Joannopoulos J, Fink Y. Thermal-sensing fiber devices by multimaterial codrawing. *Adv Mater* **2006**;*18*(7):845–9.

20. Egusa S, Wang Z, Chocat N, Ruff Z, Stolyarov A, Shemuly D, Sorin F, Rakich P, Joannopoulos J, Fink Y. Multimaterial piezoelectric fibers. *Nat Mater* **2010**;*9*(8):643–8.

21. Yan W, Noel G, Loke G, Meiklejohn E, Khudiyev T, Marion J, Rui G, Lin J, Cherston J, Sahasrabudhe A, Wilbert J, Wicaksono

I, Hoyt R, Missakian A, Zhu L, Ma C, Jaonnopoulos J, Kink Y. Single fibre enables acoustic fabrics via nanometer-scale vibrations. *Nature* **2022**;*603*:616–23.

22. Yu L, Parker S, Xuan H, Zhang Y, Jiang S, Tousi M, Manteghi M, Wang A, Jia X. Flexible multi-material fibers for distributed pressure and temperature sensing. *Adv Funct Mater* **2020**;*30*:1908915.

23. Leber A, Dong C, Chandran R, Gupta T, Bartolomei N, Sorin F. Soft and stretchable liquid metal transmission lines as distributed probes of multimodal deformations. *Nat Electron* **2020**;*3*:316–26.

24. Kiourti A, Volakis J. Stretchable and flexible E-fiber wire antennas embedded in polymer. *IEEE Antennas Wirel Propag Lett* **2014**;*13*:1381–4.

25. Du M, Huang L, Zheng J, Xi Y, Dai Y, Zhang W, Yan W, Tao G, Qiu J, So K, Ren C, Zhou S. Flexible fiber probe for efficient neural stimulation and detection. *Adv Sci* **2020**;*7*(15):2001410.

26. Cevik I, Huang X, Yu H, Yan M, Ay S. An ultra-low power CMOS image sensor with on-chip energy harvesting and power management capability. *Sensors* **2015**;*15*:5531–54.

27. Deisseroth K, Feng G, Majewska A, Miesenböck G, Ting A, Schnitzer M. Next-generation optical technologies for illuminating targeted brain circuits. *J Neurosci* **2006**;*26*(41):10380–6.

28. Boyden E, Zhang F, Bamberg E, Nagel G, Deisseroth K. Milli-second-timescale, genetically targeted optical control of neural activity. *Nat Neurosci* **2005**;*8*(9):1263–8.

29. Wang H, Wang B, Normoyle K, Jackson K, Spitler K, Sharrock M, Miller C, Best C, Liano D, Du R. Brain temperature and its fundamental properties: a review for clinical neuroscientists. *Front Neurosci* **2014**;*8*:307.

30. Brook V. Study of brain function by local, reversible cooling. *Rev Physiol Biochem Pharmacol* **1983**;*95*:1–103.

31. Tao G, Abouraddy A, Stolyarov A. Multimaterial fibers. *Appl Glass Sci* **2012**;*3*(4):349–68.

32. Polycarbonate. Wikimedia Foundation. 2022. https://en.wikipedia.org/wiki/Polycarbonate.

33. Incropera F, De Witt D. Introduction to heat transfer, 2nd ed. New York: Wiley; **1990**.

34. Commercial and Industrial-Grade Products. 2019. https://www.cactus-tech.com/wp-content/uploads/2019/03/Commercial-and-Industrial-Grade-Products.pdf.

Publisher's Note Springer Nature remains neutral with regard to jurisdictional claims in published maps and institutional affiliations.

Shaun Berry is a technical staff member in the Advanced Materials and Microsystems group at MIT Lincoln Laboratory. His current research interests are in microfluidics and electro-wetting for the development of novel devices in chem/bio, active optical systems, communications, and micro-hydraulics. He has authored or co-authored numerous papers and conference presentations in the field of microfluidics and electro-wetting. Dr. Berry received a BS degree in mechanical engineering from North-eastern University and a Ph. D. in mechanical engineering from Tufts University. As a graduate student he conducted research in fluid dynamics and the study of the electro-wetting phenomenon.

Shawn Redmond has been at MIT Lincoln Laboratory over 13 years, pursuing research in novel hyperspectral detection architectures, chemical sensing, LWIR/MWIR sensing, fibre optic lasers, laser beam combination, and novel laser media. Prior to joining Lincoln Laboratory, he was a research engineer at Lockheed Martin Aculight and Northrop Grumman Space Technology. He has authored and co-authored numerous papers and conference presentations in the fields of hyperspectral imaging, laser beam combination, high-power lasers, and rare-earth spectroscopy as well as served on the advisory committees for conferences on high power lasers and luminescence. Dr. Redmond received a BS degree in engineering physics from Oregon State University and a PhD degree in electrical engineering from the University of Michigan conducting research in rare-earth spectroscopy and scattering.

Tairan Wang is senior staff in the Advanced Materials and Microsystem group at MIT Lincoln Laboratory. His research interests center on advanced functional fibers and microsystems. Prior to joining MITLL, he was Chief Operating Officer of Advanced Functional Fabrics of America, one of the Manufacturing Innovation Institutes. Previously, he held senior leadership positions in startup companies in the fields of integrated photonics and medical devices. He is co-inventor on 17 patents and patent applications. Dr. Wang received BS degrees in physics and EECS, and a PhD in condensed matter physics from MIT.

Mordechai Rothschild is principal staff in the Advanced Technology Division at MIT Lincoln Laboratory. He has led programs in metamaterials, microfluidics, and nanofabrication, and has managed programs to develop multifunctional microsystems combining optics, mechanics, and microfluidics. Previously, he played a leading role in the development of advanced optical lithography technologies, including 193-nm and liquid-immersion lithography. He co-chaired the 2012 Lithography Workshop, and he is a member of the program committee of the International Conference on Electron, Ion, and Photon Beam Technology and Nanofabrication. He is the recipient of the 2014 SPIE Frits Zernike Award in Lithography and of the 2015 Edwin H. Land medal awarded jointly by the Society for Imaging Science and Technology and the OSA. Dr. Rothschild received a BS degree in physics from Bar-Ilan University and a PhD in optics from the University of Rochester.